In Situ Integration of Stable Glass Microdevices on Optical Fiber Tips via Ultrafast Laser 3D Nanolithography

*Shangben Jiang, Dezhi Zhu, Haoqiang Huang, Haorui Fang, Dejun Liu, Ying Wang, Yiping Wang, and Changrui Liao**

Integrating microdevices on optical fiber tips possesses significant potential for sensing, imaging, and related fields. However, their fabrication has long been constrained by incompatibility and the chemical and thermal instability of polymeric materials. This study proposes a novel fabrication strategy for stable glass microdevices in situ integrated on optical fiber based on femtosecond laser 3D nanolithography. Through optimization of siloxane materials and robust structural design, unstable organic structures can be transformed into stable glass structures. Synergizing interfacial tension with optimized contact surfaces ensures uniform shrinkage of the functional structure during annealing. The devices exhibit appreciable thermal stability and organic solvent resistance, withstanding prolonged acetone immersion. Experimental results demonstrate the high performance of the fabricated glass microdevices in optical microsystems, along with sustained stability in harsh environments. This study offers a promising approach for fabricating fiber-integrated inorganic functional structures, paving the way for significant advancements in fiber-integrated functional microdevices.

1. Introduction

With the continuous advancement of optical fiber sensing technology in recent years, functional microstructures on fiber tips have found widespread applications in sensing and imaging, offering advantages such as compact size, high sensitivity, and immunity to electromagnetic interference.[1–3] The optical fiber tip is a platform for integrating expandable micro/nanostructures and facilitates interactions between emitted light and functional structures on its end face. However, the 3D fabrication of stable functional structures in situ integrated on optical fibers remains challenging. Most polymers tend to deform and fail at elevated temperatures, and their inherent degradability further compromises the long-term performance of fiber-tip functional microdevices in harsh environments. In contrast, inorganic nanostructures, driven by their tremendous application prospects, are positioned at the forefront of both fundamental research and industrial innovation.[4–8] Among inorganic substances, silica is prominent due to its diverse applications across science, industry, and society. In particular, its remarkable mechanical robustness, high optical clarity, and strong resistance to thermal and chemical challenges significantly contribute to its widespread utility.[9–13] Several strategies, including stereolithography[14] and digital light printing,[15] have been proposed for processing glass micro/nanostructures. Although they enable the fabrication of silica components, their feature sizes are generally confined to tens of micrometers. Because these methods rely on silica nanoparticle loaded composites, high-temperature sintering is unavoidable, creating a significant challenge. Additionally, to bond silica nanoparticles into a coherent structure, a sintering process must be conducted at up to 1300 °C in a vacuum or inert atmosphere, often taking several days to complete. This sintering temperature, which exceeds the softening point of optical fibers, makes conventional additive manufacturing strategies using silica nanoparticle-loaded composites generally unsuitable for fiber-based fabrication.

Two-photon polymerization (TPP), which represents an advanced form of 3D printing, makes it possible to construct intricate 3D architectures, enabling new functionalities through the added spatial dimension.[16,17] Exceeding the limits of traditional 3D printing, this method utilizing femtosecond laser pulses with nonlinear effects achieves the fabrication of submicron-precise structures. These detailed features are vital for both effective light confinement and the enhancement of high-speed optical communications. Through direct laser writing in photoresist, TPP facilitates the single-step, precise manufacturing of optical components at micro- and nanoscales,[18–22] thereby

---

S. Jiang, D. Zhu, H. Huang, H. Fang, D. Liu, Y. Wang, Y. Wang, C. Liao
Shenzhen Key Laboratory of Ultrafast Laser Micro/Nano Manufacturing, Guangdong and Hong Kong Joint Research Centre for Optical Fiber Sensors, State Key Laboratory of Radio Frequency Heterogeneous Integration
Shenzhen University
Shenzhen 518060, China
E-mail: cliao@szu.edu.cn

S. Jiang, D. Zhu, H. Huang, H. Fang, D. Liu, Y. Wang, Y. Wang, C. Liao
Shenzhen Key Laboratory of Photonic Devices and Sensing Systems for Internet of Things, Key Laboratory of Optoelectronic Devices and Systems of Ministry of Education/Guangdong Province, College of Physics and Optoelectronic Engineering
Shenzhen University
Shenzhen 518060, China

The ORCID identification number(s) for the author(s) of this article can be found under https://doi.org/10.1002/lpor.202501110

DOI: 10.1002/lpor.202501110

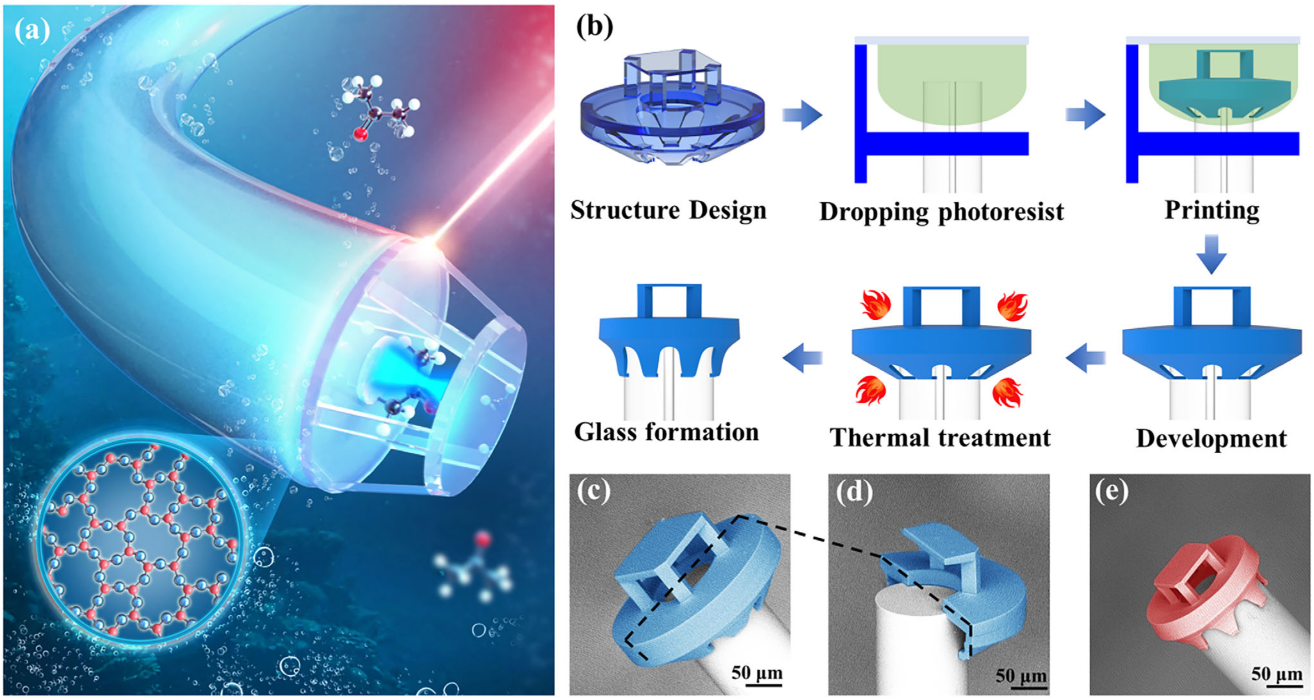

Figure 1. Ultrafast laser 3D nanolithography for in situ fabrication of fiber-integrated stable glass microdevices. a) Schematic illustration of stable glass microdevices on the fiber tip for organic solvent sensing. b) The printing and heat treatment process for fabricating stable glass microdevices on the fiber integrated. c) SEM image of the as-printed organic structure before the thermal treatment process. d) The cross-sectional view of the as-printed organic structure is shown in part (c), and e) SEM image of the glass structure after thermal treatment.

permitting the custom creation of complex optical elements. According to recent studies, polyhedral oligomeric silsesquioxanes (POSS) with a silicon-oxygen framework is suitable for printing silicon glass.[23] The hardened gel film state might impose printing constraints when using hydrogen silsesquioxanes as precursors.[24,25] Utilizing POSS and acrylic oligomer composite materials and operating under conditions that are both sinterless and low in temperature, the technology for producing fused silica micro/nanostructures through two-photon polymerization has been successfully realized.[26,27] Despite achieving outstanding optical and mechanical properties with silica glass devices produced by this method, directly manufacturing stable glass devices with functional nanostructures on optical fiber tip remains challenging. Although previous work demonstrated silica glass structures on the tips of optical fibers,[28] these structures lacked functional properties, and their potential applications remain unexplored (Table S1, Supporting Information). Additionally, during heat treatment, as the printed structure converts to its glassy phase, the bonding between the bottom layer and the substrate results in nonlinear shrinkage of the overall structure, which warrants further study.[29–32] Thus, in situ fiber-integrated functional glass microdevices with high stability still require further development for microsystem application.

In this work, we propose a fabrication strategy based on femtosecond laser 3D nanolithography that in situ integrates stable glass microdevices onto optical fibers. Acrylate-functionalized precursors serve as the foundational material and the structural design is optimized to enable integration. The synergy of interfacial tension and enlarged contact surfaces enables the fabricated devices to form a conformal interface with the fiber tip, resulting in a compact configuration. This approach ultimately enables the conversion of organic structures into stable glass architectures that offer enhanced thermal stability and durability compared to their organic counterparts. In addition, the fabricated glass microdevices exhibit robust optical performance and maintain chemical stability in harsh environments such as organic corrosive solutions, highlighting their suitability for biosensing and other microsystem applications operating under chemically complex or solvent-rich conditions. This strategy not only advances inorganic micro-/nano-fabrication but also opens avenues for designing next-generation integrated sensors, with prospective applications spanning real-time biomedical diagnostics and environmental monitoring.

2. Results and Discussion

2.1. Concept of In Situ Fiber-Integrated Glass Microdevices through Ultrafast Laser

Figure 1a schematically illustrates the concept of in situ fabricating fiber-integrated stable glass microdevices using ultrafast laser 3D nanolithography. Efforts have been made in both material selection and structural design to achieve stable glass microdevices. The photoresist employed is a unique negative formulation that comprises two critical components, namely acrylate-functionalized POSS and a photoinitiator which distinguishes it from conventional photoresists. The POSS cage, characterized by its silicon-oxygen framework architecture, provides structural robustness.[33,34] Unlike sol-gel counterparts, acrylic-functionalized components[35–37] demonstrate enhanced printability. The photoinitiator Irgacure 369 was selected to reduce the polymerization difficulty of acrylic monomers under ultrafast laser exposure. The compound was chosen based on its dual functional properties: a high rate of radical generation and a strong nonlinear absorption response. A stable and clear hybrid resin was obtained through mixing and heating the two precursor components. 3D nanoprinting was done with a 1030 nm femtosecond laser using custom-built equipment.[38–41] Figure 1b demonstrates a stable glass structure fabrication process at the fiber tip using femtosecond laser 3D nanoprinting. The resin was deposited onto the fiber tip, and the laser beam was focused into the material through an objective lens. Within the focal area, multiphoton absorption by the photoinitiator leads to the cleavage of covalent bonds and the generation of free radicals. The free radicals initiate the crosslinking of acrylic functional groups, resulting in the solidification of the resin into a stable structure.[20,42] By controlling the in-plane scanning of the laser beam with a galvanometric scanner and assisting planar stacking with a three-axis stage, 3D structures are fabricated. The printed structure is submerged in isopropanol to remove residual resin for 4 min. Afterward, through a moderate thermal treatment at 700 °C in an air environment, the printed structures were transformed into silica glass, promoting the development of continuous, densely packed silicon-oxygen network structures. Thermally induced decomposition of organic constituents liberated volatile byproducts, while oxidative conditions mediated residual carbon elimination. Stabilized glass microdevices exhibiting high resolution and structural quality were fabricated on the optical fiber tip.

The false-color scanning electron microscope (SEM) images of the as-printed structure were shown in Figure 1c,d, and the formed glass was depicted in Figure 1e. The design features a configuration that wraps around the end face to enhance its integration with the fiber tip. Furthermore, to reveal the internal details of the model more clearly, a half-section of the structure was printed, as shown in Figure 1d. The optical microscope images of the two structures are shown in Figure S1 (Supporting Information). A hole was designed at the center of the optical fiber tip to minimize the reflective surface between the fiber and the top of the structure. The notch at the base of the structure served two purposes: first, it allowed the photoresist inside the structure to be removed entirely during the development process; second, it reduced stress accumulation at the base of the structure during the heat treatment process. The glass structure after heat treatment, encapsulated at the optical fiber tip, is demonstrated in Figure 1e. The designed structure enables the device to retain structural integrity after the thermal treatment. Ultrafast laser 3D printing technology can fabricate complex models on the optical fiber tip (Figure S2, Supporting Information), thereby ensuring the complete processing of intricate structures. Above all, fiber-integrated silica glass microdevices with a high dimensional precision can be fabricated through ultrafast laser 3D nanolithography combined with structural design optimization.

2.2. Morphology and Performance Characterization of As-Printed Organic Microdevices

The optical microscopy images of as-printed organic microdevices with different heights and their corresponding reflection spectra are presented in **Figure 2a**. The reflection spectra were measured using an amplified spontaneous emission and an optical spectrum analyzer to optimize the structural parameters. The Fabry-Perot interferometers (FPIs) originate from reflections at the fiber tip and the two surfaces of the microdevice. Within the single-mode fiber, a fraction of the incident light is reflected at the fiber tip, while the remainder passes through to interact with the lower and upper surfaces of the microdevice, where partial reflections occur and return to the fiber. This interaction produces three distinct FPIs: an air cavity (FPI1) situated between the fiber tip and the lower surface, a solid cavity (FPI2) located between the two microdevice surfaces, and a hybrid cavity (FPI3) formed by the fiber tip and the upper surface. Among these, FPI3 exhibits notably weaker optical intensity compared to FPI1 and FPI2. Furthermore, the cavity length of FPI2 remains unchanged after sensor fabrication. Consequently, the air cavity was selected for signal demodulation. As observed in previous study, the stability of conventional sensors declines with an increase in base height, making it more vulnerable to toppling when subjected to external forces.[3] If the base height is excessively small, the surface tension effects during washing solution evaporation cause the structure to detach readily, ultimately reducing the fabrication yield of microdevices. Therefore, in this microdevice design, to achieve structural stability at different cavity lengths of FPI, a fixed base fully encapsulating the optical fiber tip has been selected. The relationship equation between the cavity length and the free spectral range (FSR) is $FSR = \lambda_r^2/(2nL)$, where n is the refractive index of the medium in the cavity.[43] The FSRs of the three structures were measured as 11.44, 14.48, and 19.34 nm, corresponding to wavelengths of 1498.4, 1499.7, and 1489.5 nm, respectively. From these measurements, the base heights of the three structures were determined to be 98.1, 77.7, and 57.4 µm. The deviations between the measured and designed heights remain consistent, with the top surface of the organic microdevice maintaining a good parallel alignment with the optical fiber tip across different base heights. In addition, the FPI demonstrated a significant reflection spectrum contrast of over 10 dB. The data suggest that 3D printed devices offer outstanding functionality.

To investigate the sensing performance of the as-printed organic FPI, the microdevice was immersed in glycerol solutions with varying refractive indices, and the corresponding reflection spectra are presented in Figure 2b. Throughout the measurement procedure, the test liquid occupies the open cavity, changing the internal refractive index and ultimately causing a shift in the dip wavelength of the single-mode fiber reflection spectrum. The relationship between the dip-wavelength shift ($\Delta\lambda_r$) and the variation in refractive index (Δn_0) is $\Delta\lambda_r/\lambda_r = \Delta n_0/n_0$ where λ_r is the dip wavelength, and n_0 is the refractive index. The wavelength shift of the interference dip exhibits a linear dependence on the refractive index variation. Based on this principle, the refractive index variation of a liquid sample can be determined by monitoring the optical response of the fiber-tip FPI. As shown in the upper right annotation, the refractive index values of the

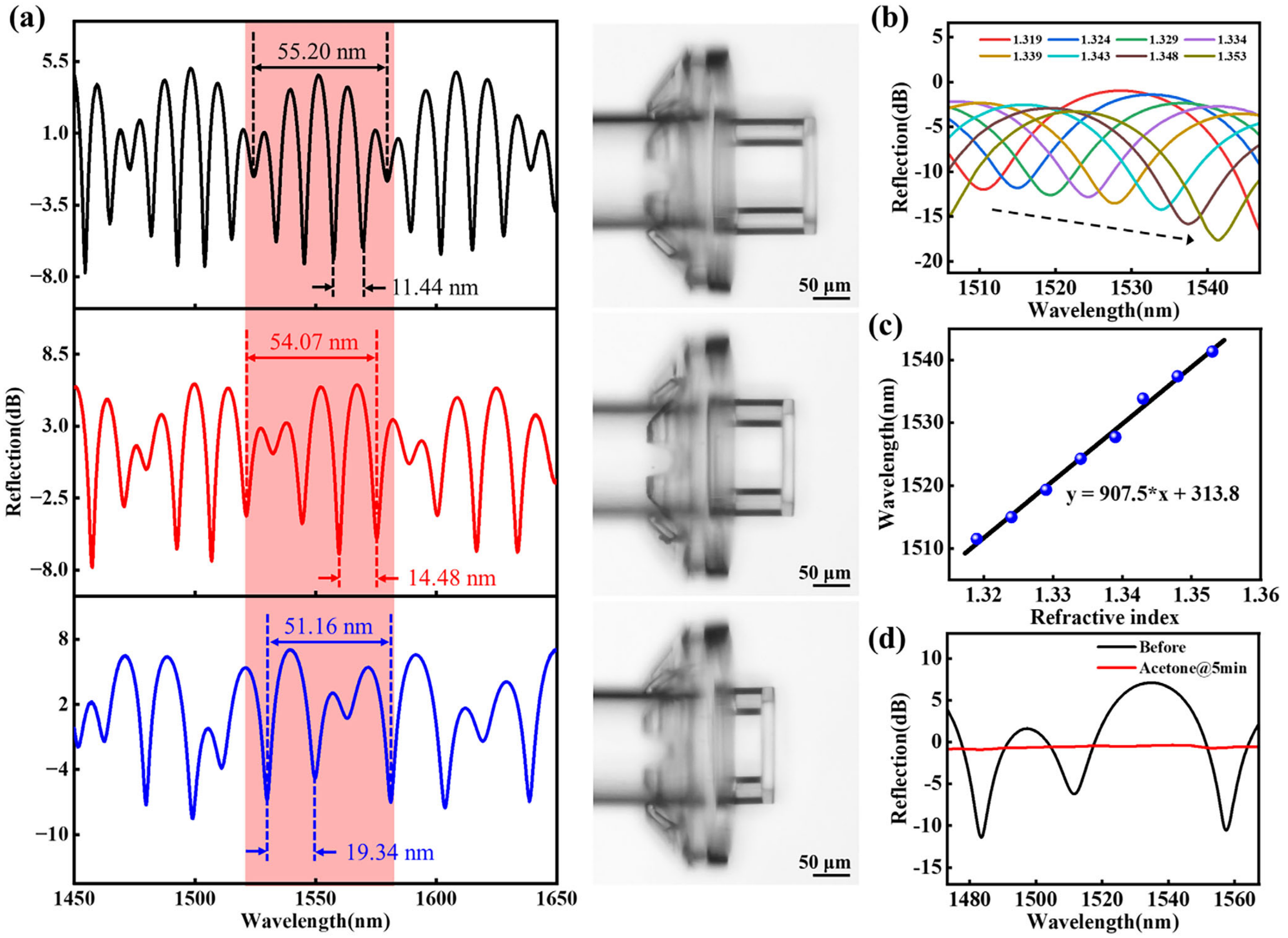

Figure 2. Morphological and performance characterization of as-printed organic microdevices. a) Optical microscopy images of as-printed organic microdevices with different heights and their corresponding reflection spectrum. b) The refractive index measurements in the index matching fluid. c) Linear fitting of the dip wavelength with different refractive index fluids. d) Stability characterization of as-printed refractive index sensor under acetone.

index-matching fluid are provided. In Figure 2c, a linear redshift of the interference dip is observed with increasing refractive index, showing a sensitivity of 907.5 nm/RIU. The as-printed structures exist in an organic-inorganic hybrid state, rendering them susceptible to organic solvent interactions. As demonstrated in Figure 2d, immersion in acetone induced significant spectral alterations, including the complete disappearance of the FPI peak. This spectral evolution confirms that despite complete encapsulation for structural fixation, organic components within the hybrid material dissolve upon solvent exposure, leading to device deformation and subsequent detachment from the fiber tip (Figure S3, Supporting Information). These findings underscore the inherent limitations of the as-printed hybrid state, which requires further research.

2.3. Formation Process of In Situ Fiber-Integrated Glass Microdevices through Ultrafast Laser

Unlike the organic-inorganic hybrid state, inorganic glasses exhibit strong resistance and high optical clarity after heat treatment. Forming fiber-integrated stable microdevices requires converting the as-printed structures into stable inorganic glass. To transform the initially printed structures into silica glass and establish a dense, continuous silicon-oxygen molecular network, the as-printed microdevices need to be heated together with the single-mode fiber in an air environment. The applied temperature caused the decomposition and release of organic compounds, and atmospheric oxygen facilitated the removal of the remaining carbon. Following heat treatment, cross-linked acrylic-functional POSS may undergo thermo-oxidative degradation, involving peroxide group formation, random chain scission, and releasing carbon dioxide, water, and hydrocarbons.[44,45] Our previous research has provided comprehensive material characterization.[28] As illustrated in Figure S4 (Supporting Information), a cylinder at the fiber tip after heat treatment, with a height of 29.3 μm and an FSR of 22.3 nm, exhibits a calculated refractive index of 1.4708, nearly identical to fused silica. Due to the adsorption force of the substrate, the printed structures may undergo anisotropic shrinkage during the thermal process, as marked in red in the schematic image in **Figure 3a**, and the comparison sample on the optical fiber tip is shown

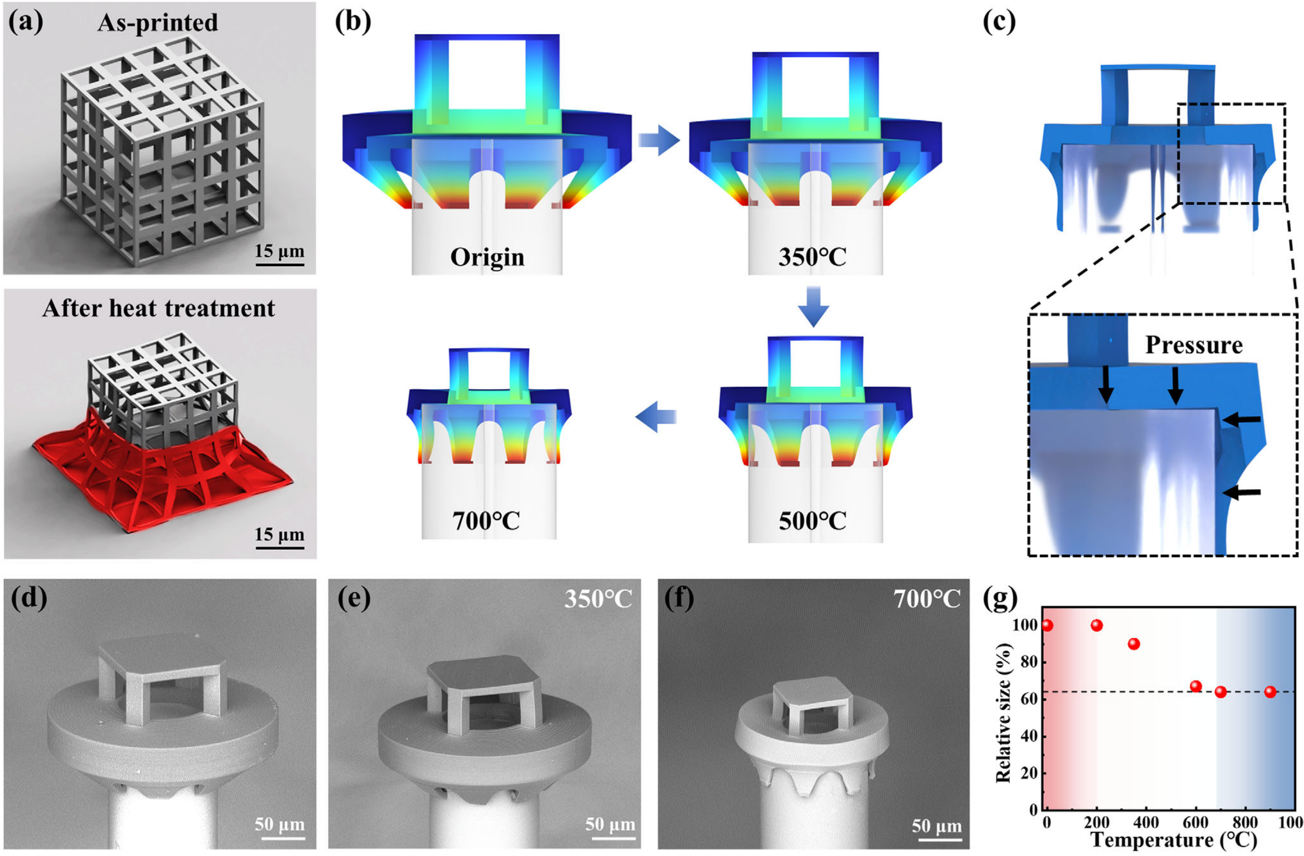

Figure 3. Formation process of in situ fiber-integrated glass microdevices through ultrafast laser. a) The schematic images of as-printed and post-annealed structures. b) The simulation results show the geometric changes of the structure during the thermal treatment, and a simplified model is employed to estimate the deformation. c) Schematic of the interface between the stable glass microdevices and fiber substrate. d) Tilt-view SEM image of the printed stable glass microdevices before thermal treatment. Tilt-view SEM image of the stable glass microdevices calcinated at e) 350 °C and f) 700 °C. g) The measured sizes of the as-printed stable glass microdevices were recorded under thermal treatment with increasing temperatures.

in Figure S5 (Supporting Information). Structural deformation, which induces heterogeneous mechanical and optical responses, is detrimental to practical device implementation.[46] The sacrificial support structures were designed to position the sensing structures at a sufficient distance from regions that are tend to nonlinear shrinkage, thereby ensuring uniform shrinkage in the critical regions. To optimize the device shrinkage effect and achieve a stable structure that tightly encapsulates the optical fiber tip, the geometric changes of the sacrificial structure during the thermal treatment process were modeled and calculated, with the shrinkage rate (SR) as the variable (Figure 3b), where the indicated temperature refers to the maximum temperature of the thermal treatment process. The shrinkage rate was defined by $SR = (S_a - S_p)/S_a$, where S_a is the size of the as-printed structure and S_p is the size of the structure after heat treatment. The simulation results clearly illustrate the shrinkage behavior of the as-printed structure. The structure consists of three parts: the bottom claw-shaped support part, the middle hollow flange part, and the top sensing part. Initially, the claw-shaped part, serving as the sacrificial substrate, connects the entire structure to the sidewalls of the optical fiber. As thermal shrinkage progresses, the contact between this part and the fiber sidewalls increases, gradually enhancing stability. The hollow flange part restricts movement in both the radial and axial directions of the fiber, ensuring tight contact between the sensing part and the fiber tip and precise alignment with the fiber core. The consequences of losing this part are illustrated in Figure S6 (Supporting Information). In this case, the shrinkage ratio at the base of the cylinder differs from that of the top reflective surface, resulting in significant deformation. At the same time, in order to achieve a better fit between the hollow flange part and the fiber tip, curvature compensation conditions are implemented on the upper surface, as depicted in Figure S7 (Supporting Information). The cross-sectional schematic of the interface between the formation glass and the optical fiber tip is shown in Figure 3c. Owing to the dimensional design, the shrunk sacrificial substrate exerted a controlled pressure on the optical fiber tip and sidewalls, thereby achieving a tightly encapsulated configuration. The optical microscopy image of microdevices after heat treatment demonstrates that the top planar structure aligns well with the fiber tip (Figure S8, Supporting Information). The dimensional evolution of as-printed structures during thermal treatment was systematically characterized from room temperature to 900 °C (Figure 3d–f). Quantitative analysis demonstrated a linear contraction of 36% in the upper region of the structures throughout the thermal conversion process (Figure 3g). Remarkably, after reaching 700 °C, the formation

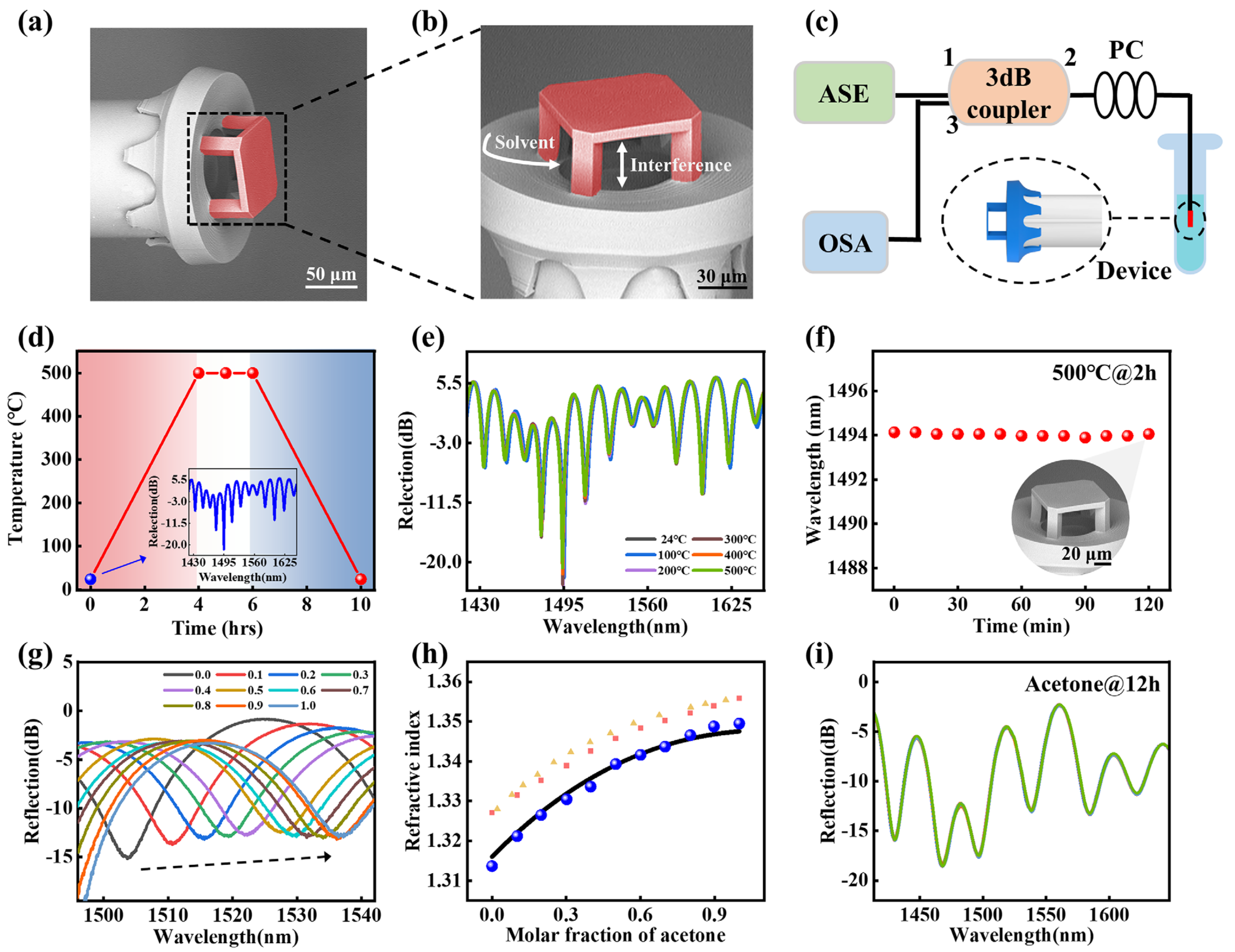

Figure 4. Optical applications of ultrafast laser-fabricated integrated stable glass microdevices. a) Colored SEM image of the fiber-tip refractive index sensor. b) Enlarged schematic representation of the refractive index measurement mechanism of the optical fiber-tip sensor. c) The experimental setup for the refractive index characterization. Temperature stability of the fabricated fiber-tip refractive index sensor: d) applied temperature-time profile, inset is the original reflection spectra of the fiber-tip microdevices, e) the reflection spectra of the fiber-tip microdevices under different temperature, f) repeated measurements of the dip wavelength at 500 °C for 2 h, insets are the SEM image of microdevices after 500 °C treatment for 2 h. g) The reflection spectrum responses of the refractive index sensor in acetone-methanol mixtures. h) Measured values of refractive index at varying molar fractions of acetone for the mixed solution. The experimental data are fitted with a third-order polynomial model. Refractive index values for mixed solutions at 589 nm, as reported by previous studies, are indicated using yellow[47] and red[48] symbols. i) Repeated measurements of the dip wavelength at acetone for 12 h.

glass microdevices exhibited high geometric stability, showing no noticeable further shrinkage. Correspondingly, the most intricate nanostructures withstood elevated temperatures without experiencing distortion or damage.

2.4. Optical Applications of In Situ Fiber-Integrated Glass Microdevices through Ultrafast Laser

Optical fibers have a softening point at 1000 °C, which makes the in situ direct integration of silica micro/nanostructures impossible when using the traditional 3D nanoprinting strategy followed by high-temperature heat treatment. The strategy for ultrafast laser fabrication of integrated stable glass microdevices, followed by heat treatment, enables their direct in situ integration. Stable glass microdevices were fabricated on the optical fiber tip to demonstrate the optical properties. As shown in **Figure** 4a, the silica microdevices consist of three components: the claw-shaped supporting base, the middle hollow flange aligner, and the open cavity with red false-color. Figure 4b presents an enlarged schematic of the sensing mechanism, featuring a suspended glass plate (74.7 × 74.7 × 6.6 µm^3) positioned 62.7 µm above the optical fiber tip, supported by four 12.5 × 12.5 µm posts. The suspended plate and fiber tip collectively constitute an open FPI. As depicted in Figure 4c, the experimental setup employs an amplified spontaneous emission, an optical spectrum analyzer and a fiber-based paddle-style polarization controller to generate arbitrary polarized light. To investigate the temperature stability of the fabricated fiber-tip silica microdevices, the optical fiber was placed in a tube furnace with an increase in temperature. Figure 4d illustrates the heating rate of the tube furnace and the inset shows the original reflection spectra of the fiber-tip microdevices. At ≈1495 nm, measurements revealed a FSR of 18 nm and a fringe visibility of over 20 dB. When increasing the applied temperature from 24 to 500 °C, there was no change in the reflection spectra of the glass microdevices (Figure 4e). After heat treatment at 500 °C for 2 h, the dip wavelength of the spectrum also did not shift and the glass microdevices maintained the intact structure, demonstrating the temperature stability of the fabricated functional structure (Figure 4f).

Owing to the inherent stability of silica glass, the glass microdevices exhibit neither swelling nor deformation in organic solvents. Consequently, they can be utilized to measure the refractive index of a binary methanol-acetone mixture, which is infeasible with organic polymer-based devices. Acetone and methanol were combined to formulate test solutions with their molar fractions adjusted in 0.1 steps. The reflection spectrum responses of the refractive index sensor in these varied acetone-methanol mixtures are depicted in Figure 4g, showing a red shift as the acetone concentration rises. The sensor was calibrated for refractive index sensing using the method described above, and the results are presented in Figure S9 (Supporting Information). By employing the previously described method, the refractive index performance of the sensor was calibrated, while the relationship between the molar fraction of acetone and the refractive index was derived from the drift of the spectral interference peak, as illustrated in Figure 4h. Refractive index values for binary methanol-acetone mixture with different molar fractions near a 589 nm test wavelength have been previously reported and are marked in the figure with yellow and red symbols.[47,48] Due to dispersion effects in the solution, the experimentally measured refractive indices are lower than those reported under a 589 nm light source. By fitting the experimental data with a cubic polynomial, the relationship between the refractive index and the acetone molar fraction in the methanol-acetone mixture is found to follow a trend consistent with that reported in the literature. Given that the glass microdevices form a continuous silicon-oxygen molecular network during the thermal process and are designed with a fixed structure clamped at the tip of the optical fiber, the fabricated micro/nano structures are anticipated to exhibit high stability. To investigate the chemical durability of the fabricated fiber-tip silica microdevices, the stable glass microdevices were immersed in a pure acetone solution (Figure 4i). After being treated in pure acetone for 12 h, the dip wavelength of the spectrum showed no shift, and the glass microdevices retained their intact structure, demonstrating the excellent chemical durability of the fabricated functional structure. Above all, the proposed 3D-printed glass refractive index sensor on the fiber tip enabled the refractive index measurement of aggressive organic solvents. Moreover, its exceptional robustness allowed for repeated measurements without significant structural deformation.

3. Conclusion

In this study, we proposed a novel fabrication strategy for ultrafast laser 3D nanolithography of fiber-integrated glass microdevices in situ. Siloxane materials were adopted as the foundational material, complemented by finite element structural analysis to ensure the stability of the glass structure. Ultrafast laser irradiation inducing nonlinear effects facilitated localized crosslinking in acrylate-functionalized precursors. The printed micro/nanostructures retained thermal stability and converted to inorganic phases after annealing at 700 °C. The glass micro/nanostructures maintain structural stability under harsh conditions, attributed to the continuous siloxane molecular networks. Finite element simulations were applied to analyze deformation patterns during the thermal treatment of complex structures, guiding the optimization of glass microdevice designs. The microdevices integrated on the optical fiber tip enabled refractive index measurements in corrosive organic solutions and exhibited improved thermal stability compared to traditional polymeric structures. On the other hand, complex structural designs present challenges for integration under specific conditions. This study contributes to the fabrication of inorganic micro/nanostructures and proposes a strategy for developing stable functional devices compatible with optical fibers.

Supporting Information

Supporting Information is available from the Wiley Online Library or from the author.

Acknowledgements

S.J. and D.Z. contributed equally to this work. This work was supported by the National Key Research and Development Program of China (2024YFB3213700), Shenzhen Science and Technology Program (Shenzhen Key Laboratory of Ultrafast Laser Micro/Nano Manufacturing ZDSYS20220606100405013), Natural Science Foundation of Guangdong Province (2022B1515120061), National Natural Science Foundation of China (T2421003, U22A2088), Postdoctoral Fellowship Program of China Postdoctoral Science Foundation (GZC20231722), LingChuang Research Project of China National Nuclear Corporation. Shenzhen Science and Technology Program (JCYJ20220818095800001).

Conflict of Interest

The authors declare no conflict of interest.

Data Availability Statement

The data that support the findings of this study are available from the corresponding author upon reasonable request.

Keywords

3D nanolithography, integrated silica, multiphoton effect, ultrafast laser

Received: May 7, 2025
Revised: August 14, 2025
Published online: August 23, 2025

---

[1] X. Shang, N. Wang, S. Cao, H. Chen, D. Fan, N. Zhou, M. Qiu, *Adv. Mater.* **2024**, *36*, 2305121.

[2] C. Liao, C. Xiong, J. Zhao, M. Zou, Y. Zhao, B. Li, P. Ji, Z. Cai, Z. Gan, Y. Wang, Y. Wang, *Light Adv. Manuf.* **2022**, *3*, 3.
[3] M. Zou, C. Liao, S. Liu, C. Xiong, C. Zhao, J. Zhao, Z. Gan, Y. Chen, K. Yang, D. Liu, Y. Wang, Y. Wang, *Light: Sci. Appl.* **2021**, *10*, 171.
[4] Y. Wang, I. Fedin, H. Zhang, D. V. Talapin, *Science* **2017**, *357*, 385.
[5] F. Han, S. Gu, A. Klimas, N. Zhao, Y. Zhao, S.-C. Chen, *Science* **2022**, *378*, 1325.
[6] K. Sun, D. Tan, X. Fang, X. Xia, D. Lin, J. Song, Y. Lin, Z. Liu, M. Gu, Y. Yue, J. Qiu, *Science* **2022**, *375*, 307.
[7] S.-F. Liu, Z.-W. Hou, L. Lin, F. Li, Y. Zhao, X.-Z. Li, H. Zhang, H.-H. Fang, Z. Li, H.-B. Sun, *Science* **2022**, *377*, 1112.
[8] F. Li, S.-F. Liu, W. Liu, Z.-W. Hou, J. Jiang, Z. Fu, S. Wang, Y. Si, S. Lu, H. Zhou, D. Liu, X. Tian, H. Qiu, Y. Yang, Z. Li, X. Li, L. Lin, H.-B. Sun, H. Zhang, J. Li, *Science* **2023**, *381*, 1468.
[9] H. Sakr, Y. Chen, G. T. Jasion, T. D. Bradley, J. R. Hayes, H. C. H. Mulvad, I. A. Davidson, E. Numkam Fokoua, F. Poletti, *Nat. Commun.* **2020**, *11*, 6030.
[10] J. G. Croissant, K. S. Butler, J. I. Zink, C. J. Brinker, *Nat. Rev. Mater.* **2020**, *5*, 886.
[11] D. Zhang, W. Xiao, C. Liu, X. Liu, J. Ren, B. Xu, J. Qiu, *Nat. Commun.* **2020**, *11*, 2805.
[12] F. Kotz, P. Risch, K. Arnold, S. Sevim, J. Puigmartí-Luis, A. Quick, M. Thiel, A. Hrynevich, P. D. Dalton, D. Helmer, B. E. Rapp, *Nat. Commun.* **2019**, *10*, 1439.
[13] A. Papadopoulos, E. Skoulas, A. Mimidis, G. Perrakis, G. Kenanakis, G. D. Tsibidis, E. Stratakis, *Adv. Mater.* **2019**, *31*, 1901123.
[14] J. T. Toombs, M. Luitz, C. C. Cook, S. Jenne, C. C. Li, B. E. Rapp, F. Kotz-Helmer, H. K. Taylor, *Science* **2022**, *376*, 308.
[15] D. G. Moore, L. Barbera, K. Masania, A. R. Studart, *Nat. Mater.* **2020**, *19*, 212.
[16] F. Kotz, A. S. Quick, P. Risch, T. Martin, T. Hoose, M. Thiel, D. Helmer, B. E. Rapp, *Adv. Mater.* **2021**, *33*, 2006341.
[17] X. Wen, B. Zhang, W. Wang, F. Ye, S. Yue, H. Guo, G. Gao, Y. Zhao, Q. Fang, C. Nguyen, X. Zhang, J. Bao, J. T. Robinson, P. M. Ajayan, J. Lou, *Nat. Mater.* **2021**, *20*, 1506.
[18] T. Liu, P. Tao, X. Wang, H. Wang, M. He, Q. Wang, H. Cui, J. Wang, Y. Tang, J. Tang, N. Huang, C. Kuang, H. Xu, X. He, *Nat. Nanotechnol.* **2024**, *19*, 51.
[19] L. Yang, H. Hu, A. Scholz, F. Feist, G. Cadilha Marques, S. Kraus, N. M. Bojanowski, E. Blasco, C. Barner-Kowollik, J. Aghassi-Hagmann, M. Wegener, *Nat. Commun.* **2023**, *14*, 1103.
[20] W. Ouyang, X. Xu, W. Lu, N. Zhao, F. Han, S.-C. Chen, *Nat. Commun.* **2023**, *14*, 1716.
[21] S. K. Saha, D. Wang, V. H. Nguyen, Y. Chang, J. S. Oakdale, S.-C. Chen, *Science* **2019**, *366*, 105.
[22] S. Kawata, H.-B. Sun, T. Tanaka, K. Takada, *Nature* **2001**, *412*, 697.
[23] P.-H. Huang, M. Laakso, P. Edinger, O. Hartwig, G. S. Duesberg, L.-L. Lai, J. Mayer, J. Nyman, C. Errando-Herranz, G. Stemme, K. B. Gylfason, F. Niklaus, *Nat. Commun.* **2023**, *14*, 3305.
[24] F. Jin, J. Liu, Y.-Y. Zhao, X.-Z. Dong, M.-L. Zheng, X.-M. Duan, *Nat. Commun.* **2022**, *13*, 1357.
[25] L.-L. Lai, P.-H. Huang, G. Stemme, F. Niklaus, K. B. Gylfason, *ACS Nano* **2024**, *18*, 10788.
[26] J. Bauer, C. Crook, T. Baldacchini, *Science* **2023**, *380*, 960.
[27] D. Zhu, S. Jiang, Y. Wang, D. Liu, W. Bao, L. Liu, J. Qu, Y. Wang, C. Liao, *APL Photonics* **2025**, *10*, 026101.
[28] D. Zhu, S. Jiang, C. Liao, L. Xu, Y. Wang, D. Liu, W. Bao, F. Wang, H. Huang, X. Weng, L. Liu, J. Qu, Y. Wang, *Nano Lett.* **2024**, *24*, 9734.
[29] J. Bauer, A. Schroer, R. Schwaiger, O. Kraft, *Nat. Mater.* **2016**, *15*, 438.
[30] A. Vyatskikh, S. Delalande, A. Kudo, X. Zhang, C. M. Portela, J. R. Greer, *Nat. Commun.* **2018**, *9*, 593.
[31] X. Zhang, L. Zhong, A. Mateos, A. Kudo, A. Vyatskikh, H. Gao, J. R. Greer, X. Li, *Nat. Nanotechnol.* **2019**, *14*, 762.
[32] D. Zhu, S. Jiang, Y. Wang, D. Liu, W. Bao, L. Liu, J. Qu, Y. Wang, C. Liao, *Int. J. Extreme Manuf.* **2025**, *7*, 035503.
[33] D. Zhou, J. Li, Q. Guo, X. Lin, Q. Zhang, F. Chen, D. Han, Q. Fu, *Adv. Funct. Mater.* **2021**, *31*, 2102074.
[34] G. Fang, H. Cao, L. Cao, X. Duan, *Adv. Mater. Technol.* **2018**, *3*, 1700271.
[35] Y. Yu, A. Prudnikau, V. Lesnyak, R. Kirchner, *Adv. Mater.* **2023**, *35*, 2211702.
[36] Z. Gan, Y. Cao, R. A. Evans, M. Gu, *Nat. Commun.* **2013**, *4*, 2061.
[37] H. Wang, W. Zhang, D. Ladika, H. Yu, D. Gailevičius, H. Wang, C. Pan, P. N. S. Nair, Y. Ke, T. Mori, J. Y. E. Chan, Q. Ruan, M. Farsari, M. Malinauskas, S. Juodkazis, M. Gu, J. K. W. Yang, *Adv. Funct. Mater.* **2023**, *33*, 2214211.
[38] D. Zhu, M. Qiao, J. Yan, J. Xie, H. Guo, S. Deng, G. He, Y. Zhao, M. Luo, *Nanoscale* **2023**, *15*, 14837.
[39] D. Zhu, J. Xie, J. Yan, G. He, M. Qiao, *Adv. Mater.* **2023**, *35*, 2211983.
[40] J. Zhang, D. Zhu, J. Yan, C.-A. Wang, *Nat. Commun.* **2021**, *12*, 6665.
[41] D. Zhu, J. Yan, J. Xie, Z. Liang, H. Bai, *ACS Nano* **2021**, *15*, 13140.
[42] S. Liu, Z. Hou, L. Lin, Z. Li, H. Sun, *Adv. Funct. Mater.* **2023**, *33*, 2211280.
[43] C. Xiong, J. Zhou, C. Liao, M. Zhu, Y. Wang, S. Liu, C. Li, Y. Zhang, Y. Zhao, Z. Gan, L. Venturelli, S. Kasas, X. Zhang, G. Dietler, Y. Wang, *ACS Appl. Mater. Interfaces* **2020**, *12*, 33163.
[44] V. V. Krongauz, *Thermochim. Acta* **2010**, *503*, 70.
[45] L. Li, R. Liang, Y. Li, H. Liu, S. Feng, *J. Colloid Interface Sci.* **2013**, *406*, 30.
[46] Y. Liu, H. Wang, J. Ho, R. C. Ng, R. J. H. Ng, V. H. Hall-Chen, E. H. H. Koay, Z. Dong, H. Liu, C.-W. Qiu, J. R. Greer, J. K. W. Yang, *Nat. Commun.* **2019**, *10*, 4340.
[47] M. Iglesias, B. Orge, M. Domínguez, J. Tojo, *Phys. Chem. Liq.* **1998**, *37*, 9.
[48] M. D. Mohammadi, M. Hamzehloo, *Fluid Phase Equilib.* **2019**, *483*, 14.